

FIRST RESULTS FROM THE DRAGONFLY TELEPHOTO ARRAY: THE APPARENT LACK OF A STELLAR HALO IN THE MASSIVE SPIRAL GALAXY M101

PIETER G. VAN DOKKUM¹, ROBERTO ABRAHAM², ALLISON MERRITT¹

Accepted for publication in ApJ Letters

ABSTRACT

We use a new telescope concept, the Dragonfly Telephoto Array, to study the low surface brightness outskirts of the spiral galaxy M101. The radial surface brightness profile is measured down to $\mu_g \sim 32$ mag arcsec⁻², a depth that approaches the sensitivity of star count studies in the Local Group. We convert surface brightness to surface mass density using the radial $g-r$ color profile. The mass density profile shows no significant upturn at large radius and is well-approximated by a simple bulge + disk model out to $R = 70$ kpc, corresponding to 18 disk scale lengths. Fitting a bulge + disk + halo model we find that the best-fitting halo mass $M_{\text{halo}} = 1.7^{+3.4}_{-1.7} \times 10^8 M_{\odot}$. The total stellar mass of M101 is $M_{\text{tot},*} = 5.3^{+1.7}_{-1.3} \times 10^{10} M_{\odot}$, and we infer that the halo mass fraction $f_{\text{halo}} = M_{\text{halo}}/M_{\text{tot},*} = 0.003^{+0.006}_{-0.003}$. This mass fraction is lower than that of the Milky Way ($f_{\text{halo}} \sim 0.02$) and M31 ($f_{\text{halo}} \sim 0.04$). All three galaxies fall below the $f_{\text{halo}} - M_{\text{tot},*}$ relation predicted by recent cosmological simulations that trace the light of disrupted satellites, with M101's halo mass a factor of ~ 10 below the median expectation. However, the predicted scatter in this relation is large, and more galaxies are needed to better quantify this possible tension with galaxy formation models. Dragonfly is well suited for this project: as integrated-light surface brightness is independent of distance, large numbers of galaxies can be studied in a uniform way.

Keywords: cosmology: observations — galaxies: halos — galaxies: evolution — Galaxy: structure — Galaxy: halo

1. INTRODUCTION

Star counts in the direction of the Andromeda galaxy (M31) have shown that it is embedded in a large, complex stellar halo with significant substructure (Ibata et al. 2001; McConnachie et al. 2009). Such halos are thought to be comprised of the debris of shredded satellite galaxies (Searle & Zinn 1978; Newberg et al. 2002; McConnachie et al. 2009), and their existence around luminous spiral galaxies is a central prediction of galaxy formation models (Bullock & Johnston 2005; Abadi, Navarro, & Steinmetz 2006; Purcell, Bullock, & Zentner 2008; Johnston et al. 2008; Cooper et al. 2010; Martínez-Delgado et al. 2010; Cooper et al. 2013).

Testing these predictions for large samples of galaxies is difficult, as star count studies are limited to relatively small distances (Barker et al. 2009; Tanaka et al. 2011). A solution to this problem is to study tidal features and stellar halos in integrated light rather than star counts, as the integrated surface brightness is independent of distance³ (see, e.g., Mihos et al. 2005; van Dokkum 2005; Tal et al. 2009; Martínez-Delgado et al. 2010; Atkinson, Abraham, & Ferguson 2013). However, conventional reflecting telescopes cannot reliably observe low surface brightness emission below $\mu_B \sim 29$ mag arcsec⁻² due to systematic errors in flat fielding and the complex point spread functions of stars (see Slater, Harding, & Mihos 2009, for an in-depth discussion of these issues).

The Dragonfly Telephoto Array (Abraham & van Dokkum 2013) is a new class of telescope that is optimized for detecting spatially-extended low surface brightness emission. The prototype Dragonfly telescope consists of eight Canon

EF 400 mm f/2.8L IS II USM telephoto lenses on a common mount. Telephoto lenses have no central obstruction and are optimally baffled. Furthermore, the specific lenses used in the array are of superb optical quality, partially owing to nano-fabricated sub-wavelength corrugations on their anti-reflecting coatings. As we show in Abraham & van Dokkum (2013) the Dragonfly point spread function has an order of magnitude less scattered light than the best reflecting telescopes. By combining eight lenses that image the same area of sky we built a “compound eye” that acts as a 40 cm f/1.0 refractor. In its default configuration, four of the lenses are equipped with SDSS g -band filters and four with SDSS r filters. The pixel scale is 2.8'' and the angular field covered by each camera is $2.6^{\circ} \times 1.9^{\circ}$.

In this *Letter* we present the first results from Dragonfly: a study of the stellar halo of the well-known galaxy M101 (a.k.a. the Pinwheel Galaxy). With a distance of 7 Mpc (Lee & Jang 2012), an absolute magnitude $r = -21.5$, and a stellar mass of $\approx 5 \times 10^{10} M_{\odot}$ (see § 4), M101 is one of the nearest massive spiral galaxies. M101 has been the subject of many detailed studies (e.g., van der Hulst & Sancisi 1988; Kenney, Scoville, & Wilson 1991; Kennicutt, Bresolin, & Garnett 2003; Mihos et al. 2012), including one of the deepest photometric investigations of the outskirts of galaxies beyond the Local Group done so far (Mihos et al. 2013).

2. OBSERVATIONS AND REDUCTION

Dragonfly is located at the New Mexico Skies observatory in Mayhill, NM. It is robotic and operates in a semi-autonomous way. A total of 35 hours of observations were obtained in 13 nights in May and June 2013. A typical M101 observing sequence consisted of nine dithered 600 s exposures with all eight cameras. The size of the dither box was typically $50' \times 50'$. As we have four slightly offset cameras per filter this provides 36 independent lines of sight per filter for

¹ Department of Astronomy, Yale University, New Haven, CT 06511, USA

² Department of Astronomy & Astrophysics, University of Toronto, 50 St. George St., Toronto, ON M5S 3H8, Canada

³ This is only true for distances where the $(1+z)^4$ cosmological surface brightness dimming is unimportant.

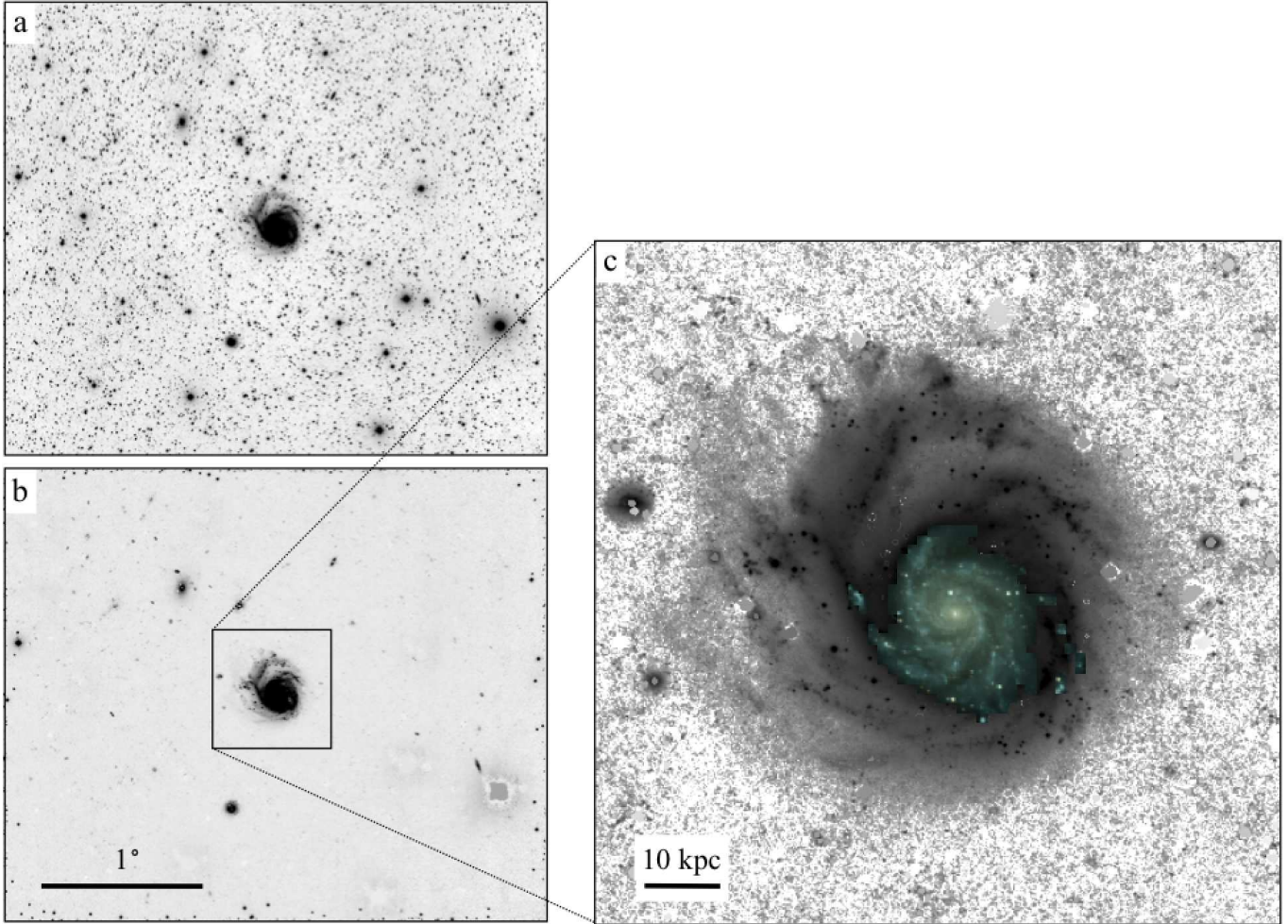


Figure 1. *a)* Dragonfly g -band image of the $3.33^\circ \times 2.78^\circ$ area centered on the galaxy M101. North is up and East is to the left. *b)* The same image, after subtraction of stars and a model for large scale ($\gtrsim 1^\circ$) background structure. Owing to the excellent PSF of Dragonfly, stars as bright as $\sim 6^{\text{th}}$ magnitude affect only a relatively small number of pixels, and can be subtracted. *c)* The $44' \times 44'$ area around M101 at high contrast. The faint spiral arms on the East side of M101 (Mihos et al. 2013) have a surface brightness of $\mu_g \sim 29 \text{ mag arcsec}^{-2}$. The color image in the center was created from the g and r exposures.

each 1.5 hr of observing time. Sky flats were taken at the beginning of each night and darks were taken throughout each night.

The data reduction followed standard procedures for imaging data, taking care to preserve the large scale faint structure in the images. After initial dark subtraction and flat fielding with night-specific calibration frames a low-order illumination correction was applied, created from a large number of dithered observations over many nights. Each frame was also corrected for the 1% – 2% gradient in the night sky emission across the field-of-view (see Garstang 1989), by subtracting a tilted plane. Combined g and r images were created for each night, using optimal weighting. The 13 images of all nights were combined for each filter, again using optimal weighting. The reduced, combined g -band image is shown in Fig. 1a.

The background in the images shows large scale variation at a level of $\approx 0.2\%$ (peak-to-peak) over the $3.3^\circ \times 2.8^\circ$ field (see Fig. 1a). As this background is independent of camera orientation and variations in the dither pattern it is most likely Galactic cirrus emission,⁴ at levels of $\gtrsim 30 \text{ mag arcsec}^{-2}$. This

large scale background was removed by fitting a third-order polynomial to a background image determined with SExtractor, aggressively masking M101 and other objects in the field. In the analysis of the surface brightness profile of M101 the average subtracted background value in a particular radial bin was added in quadrature to the uncertainty in the measured surface brightness in that bin.

Stars were removed by modeling their spatially-varying point spread function (PSF). First, large numbers of bright but unsaturated stars were used to construct average PSFs in image sections. These PSFs were then interpolated so that a PSF can be constructed for any location in the image. Next, the wings of the PSF were modeled by averaging saturated stars over the entire image. Care was taken to mask neighboring stars in an iterative way when doing the averaging, both when determining the spatially-dependent inner parts of the PSF and when constructing its wings. The background- and star-subtracted g -band image is shown in Fig. 1b.

3. THE SURFACE BRIGHTNESS PROFILE OF M101

of the M101 field, which shows a broadly similar morphology (e.g., Zagury, Boulanger, & Banchet 1999).

⁴ Some independent support for this comes from the IRAS $100\mu\text{m}$ image

The central $44' \times 44'$ of the star-subtracted g -band image, binned to a scale of $6''$ per pixel, is shown in Fig. 1c. The image shows the outer spiral arms of M101, including the faint extensions to the East that were first identified by Mihos et al. (2013). This emission, which corresponds to spiral structure seen in neutral Hydrogen emission (Walter et al. 2008; Mihos et al. 2012, 2013), has a surface brightness of $\mu_g \sim 29$ mag arcsec $^{-2}$.

We do not see coherent faint emission at larger radii. The surface brightness of M101 falls off rapidly outside of the area defined by the spiral arms, and we see no evidence for an extended stellar halo or features such as M31’s “giant stream” (Ibata et al. 2001). We quantify this visual impression with the projected surface brightness profile, shown in Fig. 2a. The profile was determined by averaging the flux in circular annuli at increasing distance from the center of the galaxy. The profile reaches $\mu_g \sim 32$ mag arcsec $^{-2}$ at $R \approx 40$ kpc, and there is no evidence for an upturn that might have indicated a regime where light from the stellar halo dominates over that of the disk. The $g-r$ color profile is shown in Fig. 2b. The galaxy becomes progressively bluer at larger radii.

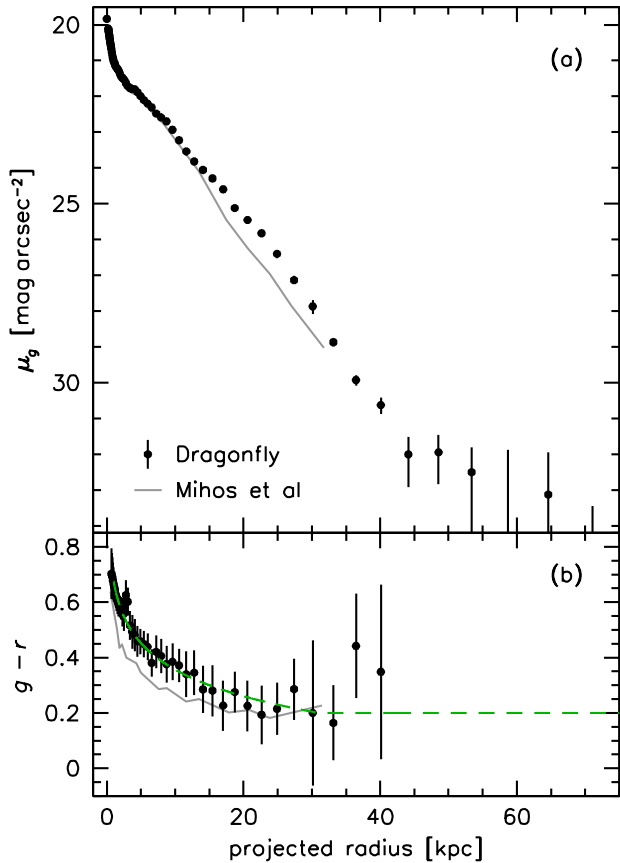


Figure 2. *a)* Radial g -band surface brightness profile of M101. The data reach $\mu_g \approx 32$ mag arcsec $^{-2}$. The grey line shows the profile of Mihos et al. (2013), converted to the g band. *b)* Color profile derived from the g and r images. The broken green line is a constrained fit to the profile (Eq. 2).

The grey line in Fig. 2a shows the surface brightness profile measured by Mihos et al. (2013), converted from μ_B to μ_g using their $B-V$ profile and Eq. 23 in Fukugita et al. (1996). Within $R = 15$ kpc the datasets agree to $\lesssim 0.05$ mag.

At $R = 20-30$ kpc there is a discrepancy, which is caused by a difference in methodology: Mihos et al. (2013) determined the median flux in each radial bin (C. Mihos, priv. comm.), whereas we use the mean. The mean and median are different at radial distances where the NE spiral arm is prominent. The grey line in the bottom panel of Fig. 2 shows the $B-V$ profile of Mihos et al. (2013), converted to $g-r$ (Fukugita et al. 1996). The profiles are offset by $\Delta(g-r) = 0.08 \pm 0.05$, where the error bar reflects the uncertainty in our zeropoint determinations only. Assuming a similar uncertainty in the Mihos et al. (2013) zeropoints and/or their conversions to standard filters, the difference is not significant.

4. MASS DENSITY PROFILE AND CONSTRAINTS ON THE M101 STELLAR HALO

4.1. Construction of the Mass Density Profile

We quantify the contribution of the stellar halo to the total mass of M101 by fitting the radial profile of M101. We first convert the observed surface brightness profile to a radial mass density profile. This step is important as M101 has a strong color gradient (Fig. 2b), and the mass-to-light (M/L) ratio correlates with color (Bell & de Jong 2001). We use the following relation between surface brightness and stellar surface density:

$$\log(\rho) = -0.4(\mu_g - 29.23) + 1.49(g-r) + 4.58, \quad (1)$$

with μ_g in mag arcsec $^{-2}$ and ρ in M_\odot kpc $^{-2}$. Equation 1 was determined from the observed relation between rest-frame $g-r$ color and M/L_g ratio for galaxies with $0.045 < z < 0.055$, $10 < \log(M/M_\odot) < 10.7$, and $0.2 < (g-r) < 1.2$ in the Sloan Digital Sky Survey DR7 (as provided by the MPA-JHU release; Brinchmann et al. 2004). The MPA-JHU relation between M/L_g and $g-r$ has a scatter of 0.12 dex and assumes a Chabrier (2003) IMF. Instead of the observed colors, which have large uncertainties at $R > 20$ kpc, we used a fit of the form

$$(g-r) = \begin{cases} -0.32 \log(R) + 0.67, & \text{if } R \leq 29 \text{ kpc} \\ 0.20, & \text{if } R > 29 \text{ kpc}. \end{cases} \quad (2)$$

This fit is indicated by the broken green line in Fig. 2b.

The mass density profile is shown in Fig. 3. The form is similar to the surface brightness profile, except for the central regions as those are more prominent in mass than in blue light. The data reach surface densities of $\lesssim 10^4 M_\odot$ kpc $^{-2}$, and a non-parametric limit on the stellar halo of M101 is that it has a stellar mass density lower than this limit at $R \gtrsim 50$ kpc.

4.2. Fitting

The profile is well-described by an exponential disk and a Sersic (1968) bulge. This fit has the form

$$\rho(R) = \rho_{0,d} \exp\left(-\frac{R}{R_d}\right) + \rho_{0,b} \exp\left[-4.85 \left(\frac{R}{R_e}\right)^{1/n}\right], \quad (3)$$

with $\rho_{0,d} = (4.40 \pm 0.11) \times 10^8 M_\odot$ kpc $^{-2}$, $R_d = 3.98 \pm 0.06$ kpc, $\rho_{0,b} = (2.24 \pm 0.08) \times 10^{10} M_\odot$ kpc $^{-2}$, $R_e = 1.67 \pm 0.12$ kpc, and $n = 2.62 \pm 0.16$. The fit is shown by the red solid line in Fig. 3a. We note that the “bulge” may in fact be more appropriately called an inner disk; as is well known M101 has a very low central velocity dispersion and spiral arms that continue into the central few arcsec (Kormendy et al. 2010).

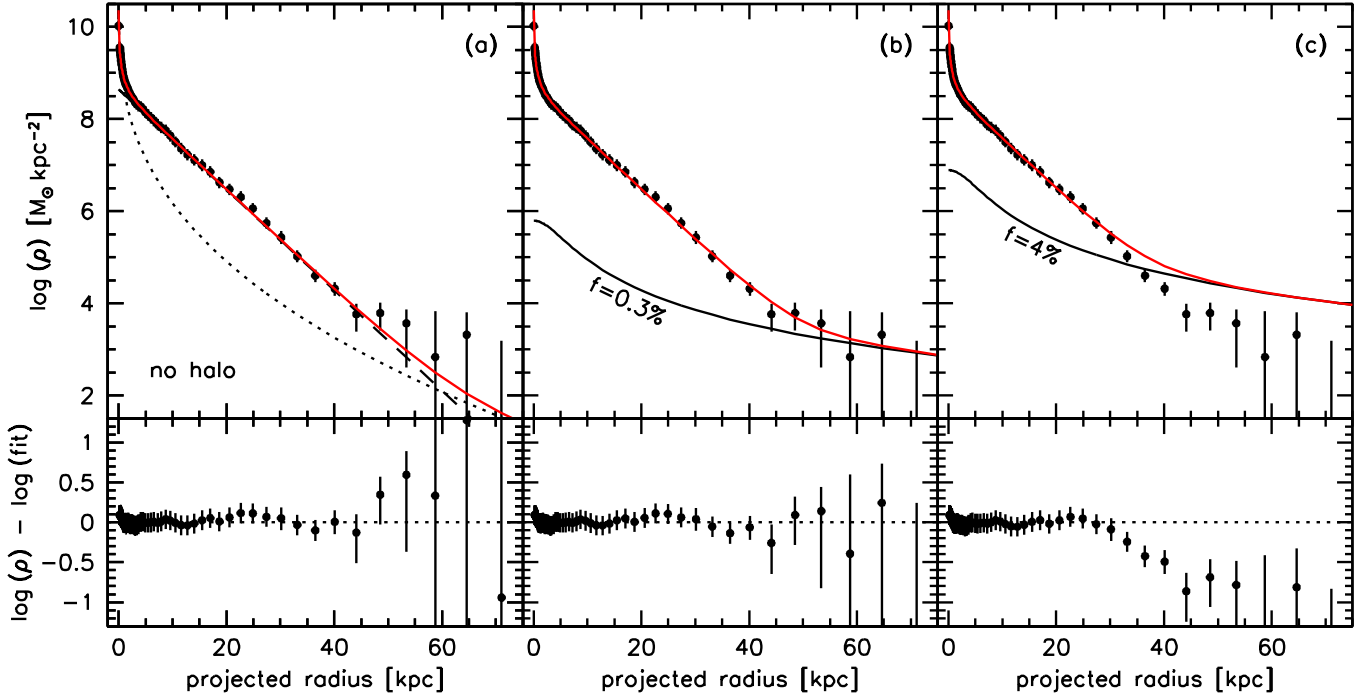


Figure 3. *a)* Mass density profile of M101. The red line is a bulge + disk fit to the profile, with the individual components indicated by broken lines. This fit provides an adequate description of the full profile, as shown by the residuals in the bottom panel. *b)* Best-fitting bulge + disk + halo fit. The best fit is obtained for a stellar halo contributing $0.3_{-0.3}^{+0.6}$ % of the total mass. *c)* Fit with a halo contributing 4% of the mass, the same as the M31 halo. This is a poor fit: the halo of M101 is much less prominent than that of M31.

The residuals from the fit are shown below panel a of Fig. 3. They are < 0.1 dex at $R = 0 - 40$ kpc and within the 1σ error bars at larger radii, confirming that there is no significant upturn in the profile. We quantify the contribution of a halo component by fitting the residuals. To parameterize the halo we adopt model “U” in the Courteau et al. (2011) analysis of the M31 light profile (their preferred model). This model is a power law:

$$\rho(R) = \rho_{0,h} \left[\frac{1 + (30/a_h)^2}{1 + (R/a_h)^2} \right]^\alpha. \quad (4)$$

The values of a_h and α are fixed to the best fits for M31, $a_h = 5.20$ kpc and $\alpha = 1.26$ (see Table 4 of Courteau et al. 2011). Fitting the normalization (i.e., the halo surface density at 30 kpc) gives $\rho_{0,h} = 7_{-7}^{+13} \times 10^3 M_\odot \text{kpc}^{-2}$. The combined disk + bulge + halo model is shown by the red line in Fig. 3b.

The total mass implied by this model of M101, integrated to $R = 200$ kpc, is $M_{\text{tot},*} = 5.3_{-1.3}^{+1.7} \times 10^{10} M_\odot$. The halo mass is $M_{\text{halo}} = 1.7_{-1.7}^{+3.4} \times 10^8 M_\odot$, and we infer that the fraction of mass in the halo is $f_{\text{halo}} = M_{\text{halo}}/M_{\text{tot},*} = 0.003_{-0.003}^{+0.006}$. This fraction is significantly lower than the halo fraction of M31: Courteau et al. (2011) find $f_{\text{halo}} \sim 0.04$ using the same decomposition method. We illustrate this difference in Fig. 3c, where we show what M101’s profile would look like if the galaxy had a 4%, M31-like halo. Such halos are clearly inconsistent with the data.

5. DISCUSSION

We have measured the surface brightness profile of M101 to ~ 18 disk scale lengths and to surface brightness levels $\mu_g \sim 32$ mag arcsec $^{-2}$. We do not find evidence for the presence of a stellar halo, or more precisely for a photometric component at large radii that can be distinguished from the disk. Taking the

halo profile of M31 as a model and fitting the normalization, we find a halo fraction of $f_{\text{halo}} = 0.003_{-0.003}^{+0.006}$.

This fraction is lower than that of M31 ($f_{\text{halo}} \sim 4\%$; Courteau et al. 2011) and also the Milky Way ($f_{\text{halo}} \sim 2\%$; Carollo et al. 2010; Courteau et al. 2011). In Fig. 4 we show the relation between stellar halo fraction and galaxy stellar mass. The stellar masses of the Milky Way and M31 were taken from McMillan (2011) and Tamm et al. (2012) respectively. For comparison, we show the relation between the accreted fraction of stars and galaxy stellar mass as predicted by numerical models that trace the light of accreted satellites in dark matter halos. This relation was derived from the data in Fig. 12b of Cooper et al. (2013) for bulge-to-total ratios $B/T < 0.9$; the relation for other B/T limits is very similar.

Interestingly, the stellar halo masses of all three galaxies are below the predicted relation, with M101 a factor of ~ 10 below the median expectation. We caution, however, that stellar halo masses are not measured in a self-consistent way in such comparisons. There is no universal definition of a stellar halo, and it is unclear whether it even makes sense to model it as a single component (see, e.g., Carollo et al. 2010). From a practical perspective it is perhaps most fruitful to test the model predictions by comparing the predicted and observed radial surface density profiles directly, or by fitting a model such as Eq. 4 with only the normalization as a free parameter. In this context it is interesting to note that the Cooper et al. (2010, 2013) models predict that stellar halos begin to dominate at $R \sim 20$ kpc and surface densities $\rho \sim 10^5 M_\odot \text{kpc}^{-2}$ – again inconsistent with the M101 observations (but not with M31).

Given the stochastic nature of accretion events and, as a consequence, the large scatter predicted in the $f_{\text{halo}} - M_{\text{tot},*}$ relation (Purcell et al. 2008; Cooper et al. 2013; Fig. 4), it is

important to build up a sample of galaxies with radial profiles reaching surface densities of $\sim 10^4 M_\odot \text{kpc}^{-2}$. Star counts with the Gemini telescope (Bland-Hawthorn et al. 2005), the Subaru telescope (Tanaka et al. 2011) and the Hubble Space Telescope (Barker et al. 2009; Radburn-Smith et al. 2011; Monachesi et al. 2013) have reached depths of $\gtrsim 30 \text{ mag arcsec}^{-2}$ but only for very nearby, low mass galaxies. Reaching those limits at distances beyond $\sim 5 \text{ Mpc}$ is exceedingly difficult as the apparent brightness of stars decreases with the square of their distance. By contrast, the integrated-light surface brightness is independent of distance, and low surface brightness-optimized telescopes such as Dragonfly can study galaxies out to the Virgo cluster and beyond.⁵ This makes it possible to construct complete samples and search for correlations of f_{halo} with other galaxy parameters. As an example, elliptical galaxies and spiral galaxies likely had different accretion histories (e.g., Guedes et al. 2011; Tal & van Dokkum 2011; Cooper et al. 2013; van Dokkum et al. 2013).

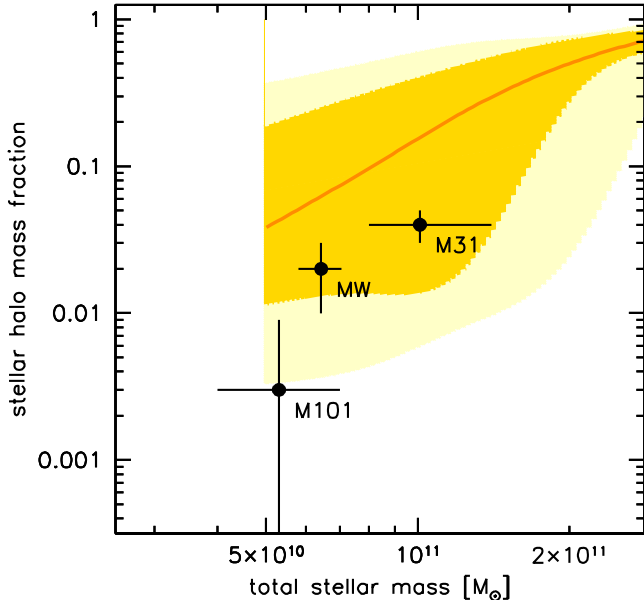


Figure 4. The mass fraction in the stellar halo as a function of the total stellar mass. The stellar halo of M101 has significantly lower mass than those of the Milky Way and M31. The orange line is the predicted median relation between the accreted mass fraction and the total stellar mass from numerical simulations (Cooper et al. 2013; see text). The yellow and brightly yellow regions indicate the 68 % and 95 % galaxy-to-galaxy variation in the simulations.

Finally, we note that halos can also be identified by their substructure, as it reflects the detailed accretion history of a galaxy (see, e.g., Fardal et al. 2008, for a discussion on M31). This history is not very informative for an individual galaxy but a large sample can provide very strong constraints on galaxy formation models (Johnston et al. 2008). To illustrate the capabilities of the Dragonfly Telephoto Array in this context, we created a simulated Dragonfly image of M31 by redshifting this galaxy to the distance of M101 (Fig. 5).

The M31 observations that were used are a combination of a Dragonfly image taken on 26 June 2013 and star count data from PAndAS (McConnachie et al. 2009; Carlberg et al.

2011). The star counts go out very far from the center of M31 but they are incomplete at small radii due to crowding. Following a similar procedure to that described in Irwin et al. (2005) Dragonfly data at $R > 0.7^\circ$ were used to tie the star count data to the integrated-light data. The combined Dragonfly + PAndAS image was redshifted to 7.0 Mpc and placed in a relatively empty region of the full-field M101 image (see Fig. 1b). This last step ensures that the noise characteristics and artifacts from the reduction are identical to the M101 data. As the scaling is identical to Fig. 1c the actual Dragonfly image of M101 can be compared directly to the simulated Dragonfly image of M31.

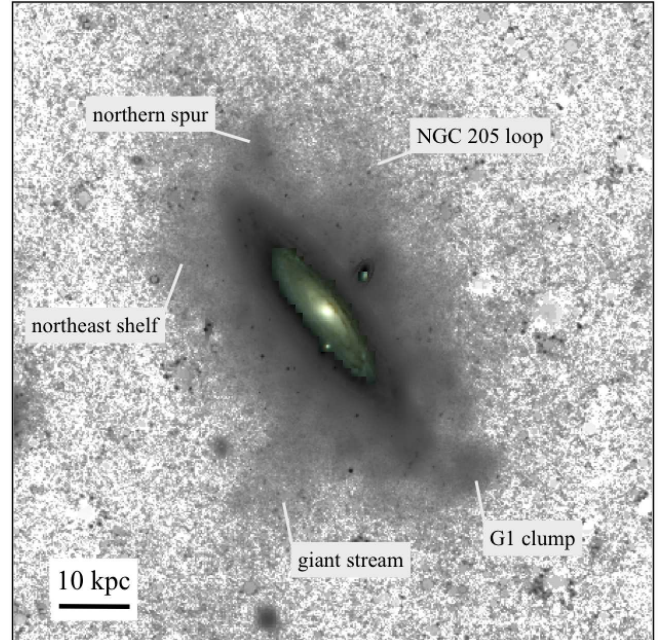


Figure 5. M31 redshifted to 7 Mpc and placed in an empty region of our M101 image. The image has the exact same scaling as Fig. 1c. Well-known features in the M31 halo are labeled; they would be easily detected with Dragonfly.

Prominent features in the M31 halo (see Fig. 1 in Ferguson et al. 2005) are labeled in Fig. 5. Remarkably, these features are all clearly visible, including the famous giant stream first identified by Ibata et al. (2001). It has been known for many decades that dramatic tidal features can be detected in integrated light; telescopes such as Dragonfly are now enabling us to detect the subtle relics of galaxy formation that should be present around every $\gtrsim L_*$ galaxy.

We are grateful to the PAndAS team for sharing their M31 star count data in digital form, to Andrew Cooper for providing us with the data to construct the model curves in Fig. 4, and to the staff at New Mexico Skies for their dedication and support. The anonymous referee is thanked for excellent comments that substantially improved the manuscript. We thank the NSF (grant AST-1312376) and NSERC for financial support.

⁵ Bland-Hawthorn et al. (2005) have pointed out that scattered light off dust grains can contribute to integrated-light measurements at very faint levels for very compact galaxies; this should not be a concern for M101.

REFERENCES

- Abadi, M. G., Navarro, J. F., & Steinmetz, M. 2006, *MNRAS*, 365, 747
- Abraham, R. G. & van Dokkum, P. G. 2013, *PASP*, in press
- Atkinson, A. M., Abraham, R. G., & Ferguson, A. M. N. 2013, *ApJ*, 765, 28
- Barker, M. K., Ferguson, A. M. N., Irwin, M., Arimoto, N., & Jablonka, P. 2009, *AJ*, 138, 1469
- Bell, E. F. & de Jong, R. S. 2001, *ApJ*, 550, 212
- Bland-Hawthorn, J., Vlajić, M., Freeman, K. C., & Draine, B. T. 2005, *ApJ*, 629, 239
- Brinchmann, J., Charlot, S., White, S. D. M., Tremonti, C., Kauffmann, G., Heckman, T., & Brinkmann, J. 2004, *MNRAS*, 351, 1151
- Bullock, J. S. & Johnston, K. V. 2005, *ApJ*, 635, 931
- Carlberg, R. G., Richer, H. B., McConnachie, A. W., Irwin, M., Ibata, R. A., Dotter, A. L., Chapman, S., Fardal, M., et al. 2011, *ApJ*, 731, 124
- Carollo, D., Beers, T. C., Chiba, M., Norris, J. E., Freeman, K. C., Lee, Y. S., Ivezić, Ž., Rockosi, C. M., et al. 2010, *ApJ*, 712, 692
- Chabrier, G. 2003, *PASP*, 115, 763
- Cooper, A. P., Cole, S., Frenk, C. S., White, S. D. M., Helly, J., Benson, A. J., De Lucia, G., Helmi, A., et al. 2010, *MNRAS*, 406, 744
- Cooper, A. P., D'Souza, R., Kauffmann, G., Wang, J., Boylan-Kolchin, M., Guo, Q., Frenk, C. S., & White, S. D. M. 2013, *MNRAS*, 434, 3348
- Courteau, S., Widrow, L. M., McDonald, M., Guhathakurta, P., Gilbert, K. M., Zhu, Y., Beaton, R. L., & Majewski, S. R. 2011, *ApJ*, 739, 20
- Fardal, M. A., Babul, A., Guhathakurta, P., Gilbert, K. M., & Dodge, C. 2008, *ApJ*, 682, L33
- Ferguson, A. M. N., Johnson, R. A., Faria, D. C., Irwin, M. J., Ibata, R. A., Johnston, K. V., Lewis, G. F., & Tanvir, N. R. 2005, *ApJ*, 622, L109
- Fukugita, M., Ichikawa, T., Gunn, J. E., Doi, M., Shimasaku, K., & Schneider, D. P. 1996, *AJ*, 111, 1748
- Garstang, R. H. 1989, *PASP*, 101, 306
- Guedes, J., Callegari, S., Madau, P., & Mayer, L. 2011, *ApJ*, 742, 76
- Ibata, R., Irwin, M., Lewis, G., Ferguson, A. M. N., & Tanvir, N. 2001, *Nature*, 412, 49
- Irwin, M. J., Ferguson, A. M. N., Ibata, R. A., Lewis, G. F., & Tanvir, N. R. 2005, *ApJ*, 628, L105
- Johnston, K. V., Bullock, J. S., Sharma, S., Font, A., Robertson, B. E., & Leitner, S. N. 2008, *ApJ*, 689, 936
- Kenney, J. D. P., Scoville, N. Z., & Wilson, C. D. 1991, *ApJ*, 366, 432
- Kennicutt, Jr., R. C., Bresolin, F., & Garnett, D. R. 2003, *ApJ*, 591, 801
- Kormendy, J., Drory, N., Bender, R., & Cornell, M. E. 2010, *ApJ*, 723, 54
- Lee, M. G. & Jang, I. S. 2012, *ApJ*, 760, L14
- Martínez-Delgado, D., Gabany, R. J., Crawford, K., Zibetti, S., Majewski, S. R., Rix, H.-W., Fliri, J., Carballo-Bello, J. A., et al. 2010, *AJ*, 140, 962
- McConnachie, A. W., Irwin, M. J., Ibata, R. A., Dubinski, J., Widrow, L. M., Martin, N. F., Côté, P., Dotter, A. L., et al. 2009, *Nature*, 461, 66
- McMillan, P. J. 2011, *MNRAS*, 414, 2446
- Mihos, J. C., Harding, P., Feldmeier, J., & Morrison, H. 2005, *ApJ*, 631, L41
- Mihos, J. C., Harding, P., Spengler, C. E., Rudick, C. S., & Feldmeier, J. J. 2013, *ApJ*, 762, 82
- Mihos, J. C., Keating, K. M., Holley-Bockelmann, K., Pisano, D. J., & Kassim, N. E. 2012, *ApJ*, 761, 186
- Monachesi, A., Bell, E. F., Radburn-Smith, D. J., Vlajić, M., de Jong, R. S., Bailin, J., Dalcanton, J. J., Holwerda, B. W., et al. 2013, *ApJ*, 766, 106
- Newberg, H. J., Yanny, B., Rockosi, C., Grebel, E. K., Rix, H.-W., Brinkmann, J., Csabai, I., Hennessy, G., et al. 2002, *ApJ*, 569, 245
- Purcell, C. W., Bullock, J. S., & Zentner, A. R. 2008, *MNRAS*, 391, 550
- Radburn-Smith, D. J., de Jong, R. S., Seth, A. C., Bailin, J., Bell, E. F., Brown, T. M., Bullock, J. S., Courteau, S., et al. 2011, *ApJS*, 195, 18
- Searle, L. & Zinn, R. 1978, *ApJ*, 225, 357
- Sersic, J. L. 1968, *Atlas de galaxias australes* (Cordoba, Argentina: Observatorio Astronomico, 1968)
- Slater, C. T., Harding, P., & Mihos, J. C. 2009, *PASP*, 121, 1267
- Tal, T. & van Dokkum, P. G. 2011, *ApJ*, 731, 89
- Tal, T., van Dokkum, P. G., Nelan, J., & Bezanson, R. 2009, *AJ*, 138, 1417
- Tamm, A., Tempel, E., Tenjes, P., Tihhonova, O., & Tuvikene, T. 2012, *A&A*, 546, A4
- Tanaka, M., Chiba, M., Komiyama, Y., Guhathakurta, P., & Kalirai, J. S. 2011, *ApJ*, 738, 150
- van der Hulst, T. & Sancisi, R. 1988, *AJ*, 95, 1354
- van Dokkum, P. G. 2005, *AJ*, 130, 2647
- van Dokkum, P. G., Leja, J., Nelson, E. J., Patel, S., Skelton, R. E., Momcheva, I., Brammer, G., Whitaker, K. E., et al. 2013, *ApJ*, 771, L35
- Walter, F., Brinks, E., de Blok, W. J. G., Bigiel, F., Kennicutt, Jr., R. C., Thornley, M. D., & Leroy, A. 2008, *AJ*, 136, 2563
- Zagury, F., Boulanger, F., & Banchet, V. 1999, *A&A*, 352, 645